nature COMMUNICATIONS

ARTICLE

Received 21 Apr 2015 | Accepted 13 Jul 2015 | Published 20 Aug 2015

DOI: 10.1038/ncomms9056

OPEN

Low-threshold amplified spontaneous emission and lasing from colloidal nanocrystals of caesium lead halide perovskites

Sergii Yakunin[1,2], Loredana Protesescu[1,2], Franziska Krieg[1,2], Maryna I. Bodnarchuk[1,2], Georgian Nedelcu[1,2], Markus Humer[3], Gabriele De Luca[4], Manfred Fiebig[4], Wolfgang Heiss[3,5,6] & Maksym V. Kovalenko[1,2]

Metal halide semiconductors with perovskite crystal structures have recently emerged as highly promising optoelectronic materials. Despite the recent surge of reports on microcrystalline, thin-film and bulk single-crystalline metal halides, very little is known about the photophysics of metal halides in the form of uniform, size-tunable nanocrystals. Here we report low-threshold amplified spontaneous emission and lasing from ~10 nm monodisperse colloidal nanocrystals of caesium lead halide perovskites $CsPbX_3$ (X = Cl, Br or I, or mixed Cl/Br and Br/I systems). We find that room-temperature optical amplification can be obtained in the entire visible spectral range (440–700 nm) with low pump thresholds down to $5 \pm 1\,\mu J\,cm^{-2}$ and high values of modal net gain of at least $450 \pm 30\,cm^{-1}$. Two kinds of lasing modes are successfully observed: whispering-gallery-mode lasing using silica microspheres as high-finesse resonators, conformally coated with $CsPbX_3$ nanocrystals and random lasing in films of $CsPbX_3$ nanocrystals.

---

[1] Department of Chemistry and Applied Biosciences, Laboratory of Inorganic Chemistry, ETH Zürich, Vladimir-Prelog-Weg 1, CH-8093 Zürich, Switzerland. [2] Laboratory for Thin Films and Photovoltaics, Empa—Swiss Federal Laboratories for Materials Science and Technology, Überlandstrasse 129, CH-8600 Dübendorf, Switzerland. [3] Institute of Semiconductor and Solid State Physics, University Linz, Altenbergerstraße 69, 4040 Linz, Austria. [4] Department of Materials, Laboratory for Multifunctional Ferroic Materials, ETH Zürich, Vladimir-Prelog-Weg 4, CH-8093 Zürich, Switzerland. [5] Materials for Electronics and Energy Technology (i-MEET), Friedrich-Alexander-Universität Erlangen-Nürnberg, Martensstraße 7, 91058 Erlangen, Germany. [6] Energie Campus Nürnberg (EnCN), Fürther Straße 250, 90429 Nürnberg, Germany. Correspondence and requests for materials should be addressed to M.V.K. (email: mvkovalenko@ethz.ch).

Recent years have seen multiple reports demonstrating outstanding optoelectronic characteristics of metal halide semiconductors with perovskite crystal structures, in the form of thin films, microcrystals and bulk single crystals[1–11]. In particular, hybrid organic–inorganic lead halide perovskites such as $MAPbX_3$ (where MA = methyl ammonium and X = Cl, Br or I, or mixed Cl/Br and Br/I systems) have shown great potential as both light-absorbing and light-emitting direct-bandgap solution-deposited semiconductors. As absorber layers, $MAPbX_3$ materials have enabled inexpensive solar cells with certified power conversion efficiencies of up to 20% (NREL efficiency chart, www.nrel.gov)[12] and highly sensitive solution-cast photodetectors operating in the visible[13], ultraviolet[14] and X-ray[15] spectra regions. Owing to their bright photoluminescence (PL), $MAPbX_3$ thin films and nanowires have been used in electrically driven light-emitting diodes[16] and as optical gain media for lasing[17–21]. We have recently shown that similarly high optoelectronic quality is also accessible in fully inorganic $CsPbX_3$ analogues, when these compounds are synthesized in the form of colloidal nanocrystals (NCs)[22]. In particular, $CsPbX_3$ NCs exhibit bright emission with PL quantum yields (QYs) reaching 90% and narrow emission linewidths of 70–100 meV (12–40 nm, for PL peaks from 410 to 700 nm, correspondingly). Precise and continuous tuning of bandgap energies over the entire visible spectral region is achievable foremost via compositional control (mixed halide Cl/Br and Br/I systems), but also through quantum-size effects. $CsPbX_3$ NCs appear to be largely free from mid-gap trap states, similar to their $MAPbX_3$ cousins[23]. Both molecular solutions of $MAPbX_3$ and colloidal solutions of $CsPbX_3$ NCs share the common feature of facile solution deposition on arbitrary substrates. Further, $CsPbX_3$ NCs are readily miscible with other optoelectronic materials (polymers, fullerenes and other nanomaterials) and feature surface-capping ligands for further adjustments of the electronic and optical properties, and solubility in various media. We also note that $CsPbX_3$ NCs are formed in the pure cubic perovskite phase, in which PbX_6 octahedra are three-dimensionally interconnected by corner-sharing. In contrast, their bulk counterparts exist exclusively in wider-bandgap one-dimensional orthorhombic phases at ambient conditions[24–26]. This disparity is most pronounced for red-emitting $CsPbI_3$ NCs that exhibit a narrow gap of down to 1.75 eV, whereas the corresponding bulk material has a *ca.* 1 eV larger bandgap and is yellow-colored and non-luminescent. A key practical advantage of $CsPbX_3$ NCs is the facile access to the blue–green spectral region of 410–530 nm via one-pot synthesis[22]. In comparison, common metal chalcogenide colloidal quantum dots such as CdSe NCs need to be extremely small (≤5 nm) to emit in the blue–green, and as-synthesized they exhibit rather low PL QYs of ≤5% due to mid-gap trap states. In addition, they are chemically and photochemically unstable, and require coating with an epitaxial layer of a more chemically robust, wider-gap semiconductor, such as CdS. On the other hand, narrow emission linewidths of *ca.* 100 meV, high PL QYs of up 90% and high photochemical stability have been achieved for Cd-chalcogenide NCs as the result of two decades of research efforts to precisely engineer core-shell morphologies with independent control of the core and shell compositions and thicknesses (for example, $CdSe_{core}/ZnCdS_{shell}$ or 'giant-shell' $CdSe_{core}/CdS_{shell}$)[27–30] and anisotropic CdSe–CdS dot-in-rod and platelet-like morphologies[31,32]. Overall, each of these two families of colloidal semiconductors—$CsPbX_3$ NCs and Cd-chalcogenide nanostructures—feature their respective advantages.

Inspired by the highly efficient PL of $CsPbX_3$ NCs, in this study we investigate the possibility of using $CsPbX_3$ NCs as an inexpensive optical gain medium. First, for thin films of $CsPbX_3$ NCs, we report the observation of amplified spontaneous emission (ASE), tunable over most of the visible range (440–700 nm) with low pump thresholds down to $5 \pm 1\,\mu J\,cm^{-2}$ and high values of modal net gain of at least $450\,cm^{-1}$. Among other colloidal semiconductor materials, such low-threshold pump fluencies have only been previously demonstrated for colloidal CdSe and CdSe/CdS nanoplatelets[33–35], whereas CdSe/ZnCdS NCs exhibit higher thresholds (from $800\,\mu J\,cm^{-2}$ in the blue to $90\,\mu J\,cm^{-2}$ in the red)[28] presumably due to stronger Auger recombination[36]. We then realize two different lasing regimes for $CsPbX_3$ NCs depending on the resonator configuration: whispering-gallery-mode (WGM) lasing using single silica microsphere resonators, conformally coated with $CsPbX_3$ NCs, and random lasing in $CsPbX_3$ NC films.

Results

Basic characteristics of $CsPbX_3$ NCs in solutions and in films. As-synthesized $CsPbX_3$ NCs, capped with oleylamine and oleic acid as surface ligands, form stable colloidal dispersions in typical nonpolar solvents such as toluene (Fig. 1a)[22]. For the spectroscopic studies in this work, we selected monodisperse samples of cubic-shaped NCs with mean sizes of *ca.* 9–10 nm (Fig. 1b). These NCs readily form uniform, compact films of sub-micron thickness on drop-casting onto a glass substrate.

The bandgap of $CsPbX_3$ NCs is controlled via compositional modulations, for example, by altering the Cl/Br ratio for the 410–530 nm range, and Br/I ratio for the 530–700 nm range

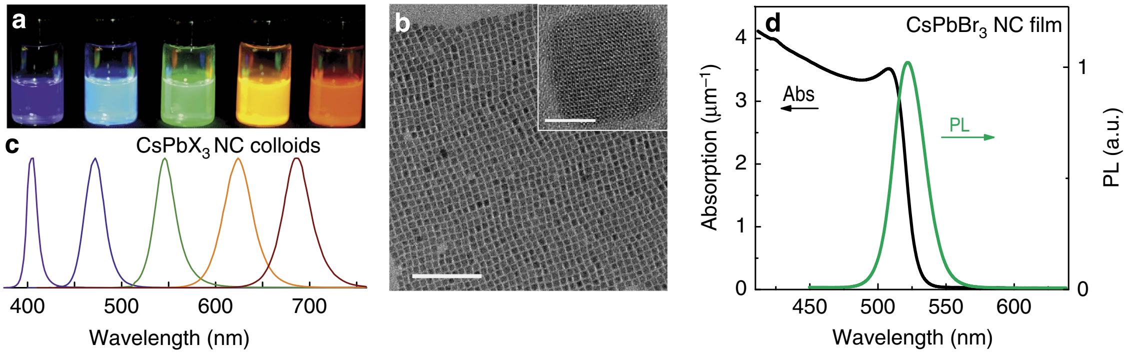

Figure 1 | Colloidal caesium lead halide perovskite NCs. (**a**) Stable dispersions in toluene under excitation by a ultraviolet lamp (λ = 365 nm). (**b**) Low- and high-resolution transmission electron microscopy images of $CsPbBr_3$ NCs; corresponding scale bars are 100 and 5 nm. (**c**) PL spectra of the solutions shown in (**a**). (**d**) Optical absorption and PL spectra of a *ca.* 400-nm-$CsPbBr_3$ NC film.

(Fig. 1c). A pronounced excitonic peak is preserved in the absorption spectrum of the $CsPbBr_3$ NC film (Fig. 1d). The absorption coefficients of the densely packed films are in the range of $(3.6–4.0) \cdot 10^4\,cm^{-1}$ (or $3.6–4.0\,\mu m^{-1}$), indicating that up to 70–80% of the pumping laser light ($\lambda = 400$ nm) is absorbed by 300–400-nm thick films. The refractive index of a $CsPbBr_3$ NC film is estimated to be 1.85–2.30 at 400–530 nm from the optical reflectance and absorption spectra (Supplementary Fig. 1). The PL from this NC film exhibits a peak with a narrow linewidth of 25 nm (110 meV), Stokes-shifted by 13 nm (57 meV) with respect to the excitonic absorption peak (Fig. 1d). The PL QYs of the same NCs in the solution reach values of up to 70–90% (for green-to-red-emitting NCs) indicating a high degree of electronic surface passivation. The PL lifetimes are very similar for solutions and for films (Supplementary Fig. 2; 1–22 ns, longer for lower-bandgap NCs). PL excitation spectrum from an NC film closely resembles the absorption spectrum (Supplementary Fig. 3).

Amplified spontaneous emission from $CsPbX_3$ NCs. Clear signatures of the ASE emission—narrowing of the emission peaks and threshold behaviour with a steep rise in intensity above the threshold—are readily obtained from 300- to 400-nm thick films produced by drop-casting colloidal solutions onto glass substrates (Fig. 2a; excitation at 400 nm with 100 fs pulses; and Supplementary Fig. 4 presenting ASE/PL on a logarithmic scale in a wider range of pumping intensities). ASE is spectrally different from PL emission; it has a narrower bandwidth of 4–9 nm (full width at half maximum, FWHM; see Supplementary Fig. 5) due to a narrow gain in bandwidth and is red-shifted by *ca.* 10 nm with respect to the PL maximum. When the ASE spectrum is overlaid with the Tauc plot of the direct-bandgap absorption (Supplementary Fig. 3), the ASE spectral maxima coincide with the end of the shallow absorption tail (Urbach tail). This red-shifted ASE may have its origins in re-absorbance during single-exciton lasing[28,29] or in the excitonic binding energies in the bi-excitonic optical gain mechanism[34,37]. Similar to PL spectra, ASE can be obtained in the whole visible spectral region by varying the composition of $CsPbX_3$ NCs (Fig. 2b). The threshold for building ASE is *ca.* $5 \pm 1\,\mu J\,cm^{-2}$ (Fig. 2c) for $CsPbBr_3$ perovskite NCs, and generally falls in the range of $5–22\,\mu J\,cm^{-2}$ for all other compositions (Supplementary Fig. 6). Notably, the ASE linewidth increases for samples with a lower ASE threshold suggesting that a larger portion of the emission falls within the optical gain conditions, enlarging the optical gain bandwidth.

In addition to the ASE threshold, the net modal gain is an important figure-of-merit that, from a practical point of view, indicates the efficiency of light amplification in the material and the quality of the resonator needed for achieving lasing[38]. Optical gain can be measured by using the variable stripe length method[39], where the excitation light is shaped into a line of variable lengths on the sample surface (see the schematics in the inset of Fig. 2d and a photograph of the emitted light in

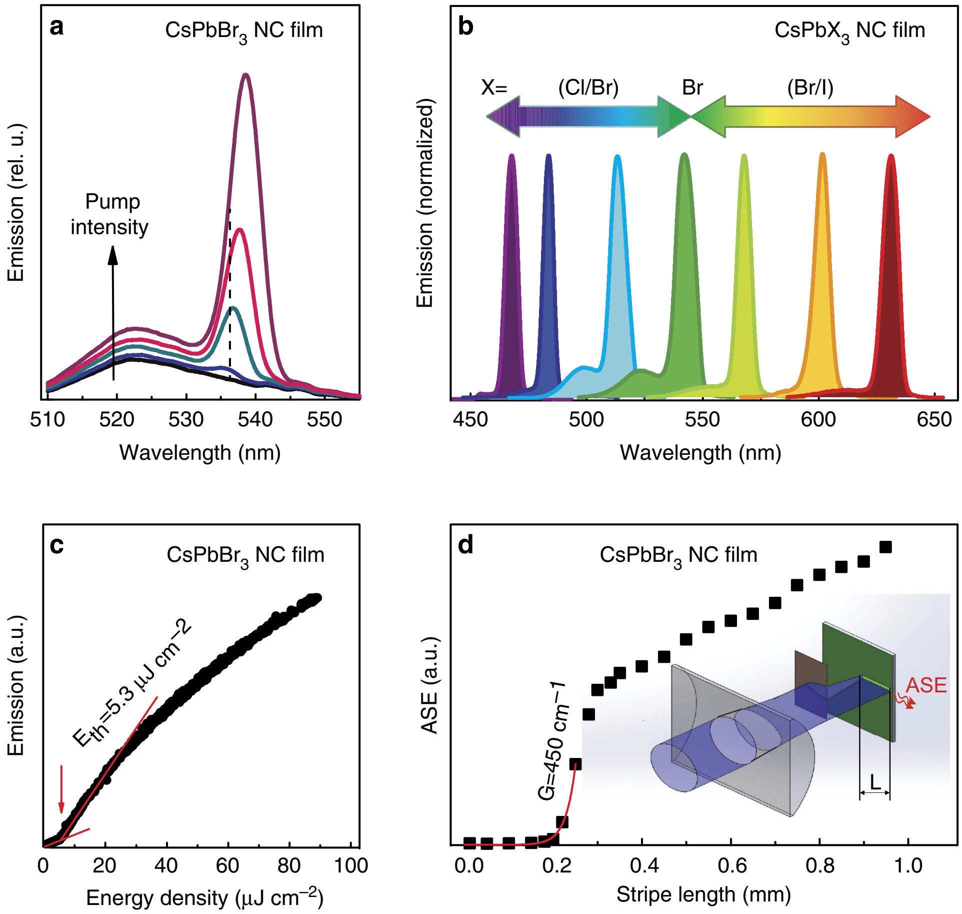

Figure 2 | ASE spectra from thin films of $CsPbX_3$ NCs. (**a**) Pump-fluence dependence of the emission from a $CsPbBr_3$ NC film (pumping intensity range was $3–25\,\mu J\,cm^{-2}$). (**b**) Spectral tunability of ASE via compositional modulation. (**c**) Threshold behaviour for the intensity of the ASE band of the $CsPbBr_3$ NC film shown in (**a**). (**d**) Variable stripe-length experiment for estimation of modal net gain for the $CsPbBr_3$ NC film. All spectra were excited at $\lambda = 400$ nm with 100 fs laser pulses.

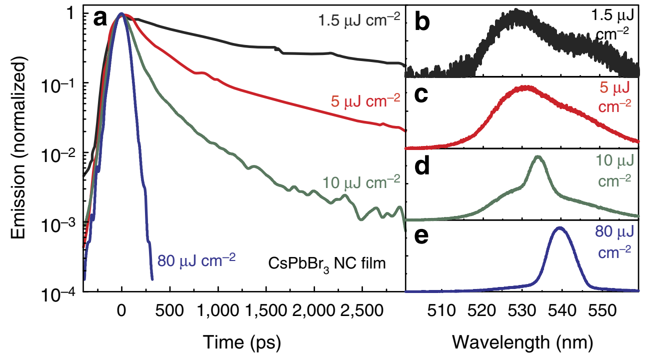

Figure 3 | Time-resolved measurements from the CsPbBr$_3$ NC film. (**a**) Decay traces at pump fluences varied from subthreshold to well above ASE threshold values with emission recorded at ASE peak wavelengths. (**b**–**e**) The corresponding full emission spectra.

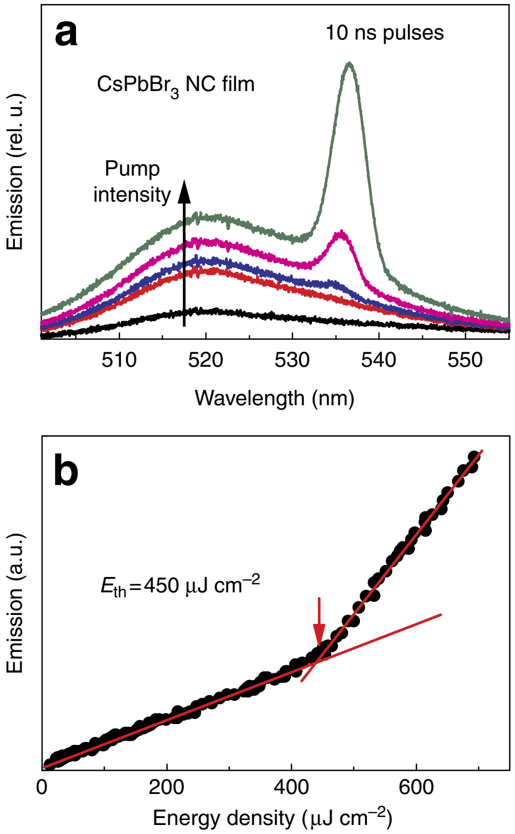

Figure 4 | ASE from CsPbBr$_3$ NC film under nanosecond excitation. (**a**) Evolution of the emission spectra with the increase of pumping fluence and (**b**) corresponding dependence of the emission at 535 nm on pump fluence. Spectra were excited at $\lambda = 355$ nm with 10 ns laser pulses.

Supplementary Fig. 7), and the emission intensity is then measured as a function of stripe length, L. When the stripe length reaches the threshold value where propagation losses are compensated by the optical amplification, the PL spectrum starts to show an additional ASE component that grows with stripe length (see Fig. 2d and corresponding spectra in Supplementary Fig. 8). The threshold region can be fitted with the model of net modal gain (G): $I = \frac{A}{g}(e^{GL} - 1)$, yielding high values of G ranging from 450 to 500 cm^{-1}. Considering these gain values, the build-up time for ASE was estimated to be 140 fs, considerably shorter than the ASE threshold lifetime of 300 ps.

Another characteristic and expected feature of ASE, seen in time-resolved experiments (Fig. 3), is the acceleration of radiative recombination due to switch from individual to collective emission. For CsPbBr$_3$ NC films in this work, at excitation intensities lower than the ASE threshold (<2 μJ cm^{-2}; Fig. 3b), typical PL lifetimes of several nanoseconds are observed with nearly single-exponent behaviour. Well above ASE thresholds (80 μJ cm^{-2}; Fig. 3e), ASE lifetimes of 60 ps were estimated, again with clean, single-exponent line shape. At the ASE threshold, an ASE lifetime of 300 ps can be roughly estimated from a bi-exponential fit assuming competing ASE and PL processes. A ‘quasi-continuous wave’ regime of excitation can be observed with pumping pulses of longer duration than this ASE lifetime[27], though at the expense of higher overall pumping fluence to maintain the same instant excitation intensity over the whole pulse duration. Such pulses can be provided by conventional, inexpensive nanosecond lasers. In this case, with a 300-ps ASE lifetime at 5–10 μJ cm^{-2} femtosecond pumping thresholds, we estimate a threshold fluence of 150–300 μJ cm^{-2} for 10-ns excitation pulses. In close agreement, ASE thresholds of 400–500 μJ cm^{-2} were observed experimentally (Fig. 4).

Whispering-gallery-mode lasing from CsPbX$_3$ NCs. Effective optical feedback from a high-quality optical resonator is needed to obtain lasing. In this regard, commercially available silica microspheres can serve as circular cavities in which the emitted light orbits around the circumference due to total internal reflection (Fig. 5a, inset). The resulting cavity modes are known as WGMs. WGM lasers can be conveniently observed by the adhesion of solution-processed lasing material onto the surface of the microspheres[17,40,41]. The great utility of microsphere resonators for research purposes stems from their extremely high and wavelength-independent Q factors of up to 10^9 (describing the degree of feedback of the cavity), and their rather isotropic leakage of the emitted light. In this work, we obtained well-resolved lasing modes with pumping threshold behaviour using 15 μm (Fig. 5a) and 53 μm (Supplementary Fig. 9) spheres, with intermodal distances dependent on the sphere diameter (the larger the sphere, the smaller the spacing). All spectra were excited at the wavelength 400 nm with 100 fs laser pulses. The observed linewidths of lasing modes (0.15–0.20 nm) are limited primarily by the resolution of the spectrometer used for detection. We note that the spectra presented herein were collected from single microspheres using a microscope objective. In contrast, when the emission from several spheres was integrated, lasing modes were often indistinguishable due to the small but essential standard size-deviation of the spheres of *ca.* 0.5–1%.

Random lasing from CsPbX$_3$ nanocrystals. Lasing can also be observed without optical resonators, namely when the required optical feedback is provided via light scattering induced by intrinsic disorder in the lasing medium, leading to so-called random lasing[42]. Light diffuses in highly scattering media and randomly forms closed loops causing random fluctuations of lasing modes. Scattering occurs, for instance, on the aggregates of NCs, and is clearly pronounced in thicker films of several microns. Since the path of the light is unique and irreproducible, so are the lasing modes (Fig. 5b) generated by each shot of the pumping laser. For the CsPbX$_3$ NC films investigated in this work, the modes appear to be fully stochastic and their distribution for 256 consecutive laser shots is presented in Fig. 5c.

The multiple emission spectra expressed as a function of wave vector in k space, shown in Fig. 5c, can be Fourier transformed into

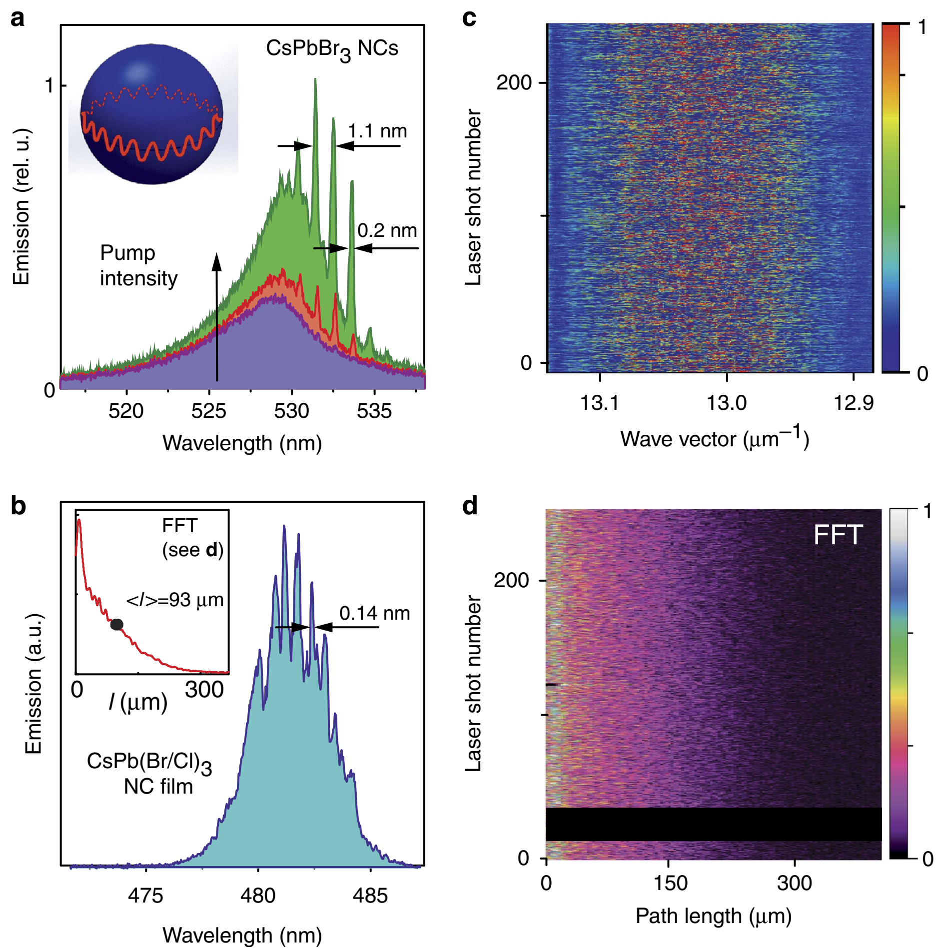

Figure 5 | Lasing in perovskite $CsPbX_3$ NC films. (**a**) Evolution from PL to whispering-gallery-mode (WGM) lasing with increasing pump intensity in a microsphere resonator of 15 μm in diameter, covered by a film of $CsPbBr_3$ NCs. (**b**) Single pump laser shot mode structure of random lasing from $CsPb(Br/Cl)_3$ NC film. The inset shows path-length distribution averaged over 256 pump laser shots. (**c**) Stochastic mode distribution in a series of 256 pump laser shots (PL background emission is subtracted). (**d**) Fast Fourier transform (FFT) of (**c**).

a corresponding optical path-length distribution (Fig. 5d). The averaged distribution of path length, *l*, over 256 shots is presented in the inset of Fig. 5b. The mean path length, $<l> = 93 \pm 5\,\mu m$, is obtained by integral averaging over the path-length range of 0–300 μm. The criterion for Anderson localization, $k<l> \approx 10^3$, is much larger than unity, pointing to the case of weakly scattering random lasing. The medium is rather transparent and shows no apparent effects from film imperfections such as cracks and pinholes. The lasing threshold is of the same order of magnitude as ASE threshold discussed above. Due to the strong increase in intensity of Rayleigh scattering with decreasing wavelength ($I \propto \lambda^{-4}$), aggregation-induced scattering and hence random lasing is most pronounced in blue-emitting samples, such as the one shown in Fig. 5b.

Discussion

Considering the colloidal nature of $CsPbX_3$ NCs, the most relevant comparison to be drawn is with strongly quantum-confined Cd-chalcogenide-based colloidal NCs. After the first demonstration of optical gain and stimulated emission from colloidal CdSe NCs (emission at 620 nm) in 2000 (ref. 37), colloidal NCs have been considered as an eventual alternative to more expensive epitaxial group III–V materials (for example, InGaN, GaAsP and InGaAs). The green spectral region is especially difficult to access by III–V compounds[43]. For this reason, the size-tunable emission of Cd-chalcogenide-based materials is highly appealing, but still lacks stability in the blue spectral region (≤ 500 nm)[29]. So far, the lowest pumping thresholds of Cd-based quantum dots (QDs) have been reported for specially engineered CdSe/ZnCdS core-shell structures, ranging from $90\,\mu J\,cm^{-2}$ for red QDs to $800\,\mu J\,cm^{-2}$ for blue QDs with single-exciton nature of the optical gain[28]. Recently, a large step forward was made by introducing pristine CdSe and core-shell CdSe/CdS nanoplatelets[35,44,45], showing the lowest ASE thresholds for inorganic colloidal nanomaterials obtained to date ($6\,\mu J\,cm^{-2}$ at 520 nm and $8\,\mu J\,cm^{-2}$ at 635 nm)[34,35]. Furthermore, in such atomically flat CdSe nanoplatelets, where bandgaps are tunable stepwise by adjusting the number of unit cells in platelet thickness, only discrete emission wavelengths were so far demonstrated and ASE had not been reported below 510 nm. Overall, in Cd-chalcogenide-based systems, emission wavelength tuning is almost exclusively achieved via quantum-size effects. On the contrary, in this study rather large $CsPbX_3$ NCs (9–10 nm) with weak to no quantum confinement were chosen and the emission was found to be freely adjustable via compositional tuning (that is, by the halide ratio). Such convenient compositional tuning is not easily accessible in Cd-chalcogenide NCs. In experiments on smaller $CsPbBr_3$ NCs with pronounced quantum-size effects, by up to an order of magnitude higher ASE thresholds were observed. Thus, a clear complementarity is seen between weakly confined $CsPbX_3$ NCs (performing best in the blue–green with $\leq 10\,\mu J\,cm^{-2}$ blue ASE thresholds) and strongly confined Cd-chalcogenide-based materials (performing best in the green–red with $\leq 10\,\mu J\,cm^{-2}$ ASE thresholds for red CdSe/CdS platelets). For a completely unbiased comparison, we have reproduced the synthesis of CdSe and core-shell CdSe/CdS nanoplatelets described by She *et al.*[35], and observed same low thresholds of 7–15 $\mu J\,cm^{-2}$ (Supplementary Figs 10 and 11) under the same testing conditions as applied here for $CsPbX_3$ NCs using femtosecond excitations. For nanosecond excitation pulses (Fig. 4), ASE thresholds for $CsPbX_3$ NCs rise to $\sim 0.45\,mJ\,cm^{-2}$ (and $1\,mJ\,cm^{-2}$ for CdSe/CdS nanoplatelets; see Supplementary Fig. 12). Low ASE thresholds in $CsPbX_3$ NCs are also assisted by an extremely large absorption cross-section (σ). For $CsPbBr_3$ perovskite NCs, we estimated $\sigma = 8 \times 10^{-14}\,cm^2$ (or $8\,nm^2$), that is almost two orders of magnitude larger than typically reported for CdSe QDs[46], and similar to CdSe nanoplatelets[47], emitting in the same wavelength range (green). No continuous-wave ASE could be observed at room temperature or down to 80 K for neither $CsPbX_3$ NCs nor for Cd-chalcogenide platelets, up to excitation levels causing photo-damage of the samples.

A comparison of our results for $CsPbX_3$ NCs with reports on closely related solution-deposited hybrid perovskite $MAPbX_3$ films and microcrystals points to rather similar ASE thresholds (Supplementary Table 1)[17–20]. $MAPbX_3$ films were also reported to exhibit random lasing[48], lasing from vertical cavities[20] and from spherical resonators[17] and WGM lasing[19]. The comparably good performance of $CsPbBr_3$ NCs indicates that their high surface area does not impede their optical properties. Also the solution-processed organic semiconductor materials exhibit similar ASE thresholds under similar testing conditions (no cavity, plane wave-guiding films)[49]. So far, in only a few examples of vacuum-deposited organic semiconductors[50] and epitaxial multiple-quantum-well structures[51] were lower, sub-$\mu J\text{-}cm^{-2}$ ASE thresholds demonstrated, but usually with an order of magnitude lower optical gain values. At the time of the submission of this work, much lower thresholds ($0.22\,\mu J\,cm^{-2}$) were reported by Zhu *et al.*[21], for lasing from $MAPbI_3$ wires, highlighting also the morphological effects (wire acts as a single-mode waveguide and laser resonator) and suggesting that future studies should focus on engineering $CsPbX_3$ wire-like morphologies with dimensions comparable to the wavelengths of light. As a first step in this direction and due to the lack of reports on bulk-like $CsPbX_3$, we have prepared $CsPbX_3$ polycrystalline films (with crystalline domain sizes of several μm) and individual microcrystals simply by drop-casting from dimethylformamide solutions and inspected their PL/ASE characteristics. NCs and microcrystals of the same composition exhibit nearly identical PL peak wavelengths and linewidths, and radiative lifetimes (Supplementary Fig. 13). ASE thresholds of polycrystalline films were by an order of magnitude higher, but this may well be caused also by the difficult-to-control, suboptimal for ASE build-up morphologies of these films. Similarly to $CsPbX_3$ NCs, the ASE peaks were found to be red-shifted with respect to the PL maxima (Supplementary Fig. 14). For selected large microcrystals (100–150 μm) clear WGM lasing modes were observed as well (Supplementary Fig. 15). No wire-like morphologies could be found for direct comparison with $MAPbI_3$ wires. Overall, we conclude that among the three distinct cases—small $CsPbX_3$ QDs (4–8 nm, chemically unstable), $CsPbX_3$ NCs (10 nm) and $CsPbX_3$ microcrystals—the NCs exhibit the best balance between optical performance (having generally the lowest ASE thresholds) and chemical versatility (exhibiting facile solution processing, and easily adjustable film thickness and morphology for obtaining various lasing regimes).

At present, we cannot fully answer the remaining question of this study—the exact mechanism for optical gain. This is also an open question in the $MAPbX_3$-related literature. To speculate on this matter for $CsPbX_3$ NCs, the observed red shift of the ASE peaks with respect to PL maxima can be explained by ether bi-excitonic lasing (due to binding energy of bi-exciton)[37] or by self-absorption in the case of a single-exciton gain[28,29]. We also evaluated the average density of excitons per each NC ($<N>$, for details, see Supplementary Note 1) at the ASE threshold and found $<N> = 0.5 \pm 0.15$. Expected theoretical values of $<N>$ are 0.5 for single-exciton gain[29] and 1 for bi-excitonic mechanism[37,52]. Increase of QY with pump intensity (Supplementary Fig. 16) might be another plausible evidence for single-exciton gain, as QY should decrease when Auger recombination is limiting the ASE (typically observed for bi-excitonic gain).

In summary, perovskite $CsPbX_3$ NCs, synthesized via a simple one-step reaction between PbX_2 and Cs-oleate in nonpolar solvent media, are particularly promising for achieving ASE/lasing in blue and green spectral regions. Optical gain is demonstrated here at room temperature for pulse durations of up to 10 ns, corresponding to the quasi-continuous wave (quasi-cw) excitation regime with low ASE threshold values down to $5\,\mu J\,cm^{-2}$. High optical gain values of up to $450\,cm^{-1}$ allow for obtaining resonant conditions for lasing either by coating $CsPbX_3$ NCs onto spherical microresonators or via random lasing mediated by light scattering on NC aggregates. Random lasing, arising from the combined effect of wave guiding and light scattering in the optical gain medium of densely packed aggregates of $CsPbX_3$ NCs, does not require an ultraprecise cavity as in conventional lasing. This not only provides the obvious technological advantage of facile and inexpensive fabrication, but also enables various niche applications such as displays and lighting, benefitting from the broad spectral angular distribution of the random lasing[42,53]. Another promising area of application for random lasers, benefitting from the broad ASE spectrum, is as the light source in optical coherence tomography where it is critical to keep optical coherence moderately low but controlled[54,55]. Random lasing in the weak-scattering regime, where the spectral distribution of lasing modes is unique for each laser shot, can serve as a physically based method for random number generation and in cryptography[56].

Methods

Preparation of $CsPbX_3$ NCs and microcrystalline films. $CsPbX_3$ NCs were synthesized as described in our recent report[22]. The crude solution was cooled down with water bath and aggregated NCs were separated by centrifuging for 3 min at 11,000 r.p.m. After centrifugation, the supernatant was discarded, the particles were redispersed in 0.3 ml hexane and centrifuged again for 4 min at 12,000 r.p.m. After repeating the previous step one more time, the precipitate was redispersed in 0.6 ml toluene, and 0.2 ml acetonitrile was added for precipitation. The NCs were centrifuged again for 4 min at 12,000 r.p.m., and after this, the supernatant was discarded and the precipitate was redispersed in toluene. Thin films of $CsPbX_3$ NCs were obtained by drop-casting 10–50 μl of $CsPbX_3$ NC solution at ambient conditions onto glass substrates, followed by drying at ambient conditions. For coating $CsPbX_3$ NCs onto silica microspheres, water-dispersed 15- and 53-μm silica microspheres (http://www.microspheres-nanospheres.com) were first drop-cast onto a hot glass substrate, followed by drop-casting of $CsPbX_3$ NCs. For preparing microcrystalline films, PbX_2 and CsX were dissolved in dimethylformamide, and then drop- or spin-cast onto a glass substrate followed by heat treatment at 150 °C. Alternatively, films of PbX_2 can be converted into $CsPbX_3$ on dipping into Cs-halide solutions.

Characterization of $CsPbX_3$ NC solutions and films. UV-Vis absorption and reflection spectra of the NC films were collected using a Jasco V670 spectrometer equipped with an integrating sphere. Steady-state PL emission and excitation spectra were acquired with a Fluorolog iHR320 Horiba Jobin Yvon spectrofluorometer, equipped with Xe lamp and a photomultiplier tube (PMT) detector. PL lifetime measurements were performed using a time-correlated single-photon counting setup, equipped with SPC-130-EM counting module (Becker & Hickl GmbH) and an IDQ-ID-100-20-ULN avalanche photodiode (Quantique) for recording the decay traces. The emission of the perovskite NCs was excited by a 400-nm 100-fs laser pulses with a repetition of 1 kHz synchronized to time-correlated single-photon counting module through an electronic delay generator (DG535 from Stanford Research Systems). Transmission electron microscopy images were recorded using a JEOL JEM-2200FS microscope operated at 200 kV. For the thickness determination of the films, an AlphaStep D-120 profilometer was used.

ASE and lasing experiments. These experiments were performed with excitation light from nanosecond and femtosecond lasers. All experiments were conducted at room temperature. The femtosecond laser system consisted of an oscillator (Vitesse 800) and an amplifier (Legend Elite), both from Coherent Inc., with a frequency-doubling external beta barium borate (BBO) crystal; it yielded 100 fs pulses at 400 nm, with a repetition rate of 1 kHz and pulse energy of up to 4 μJ. The laser beam profile had a TEM_{00} mode with a 1-mm FWHM diameter. Laser power was measured by a LabMax-TOP laser energy meter (Coherent Inc.) with a nJ-measuring head. For variable stripe length (VSL) experiments, the beam was focused into a stripe by a cylindrical lens with a focal length of 75 mm. The nanosecond laser system was a Quanta-Ray Pro 230-50 (Spectra-Physics), frequency tripled to 355 nm, with a pulse duration of 10 ns and a top-hat beam profile focused to a spot of 1.5 mm in diameter with a pulse energy of up to 30 μJ. To resolve the spectrally sharp lasing peaks, the optical emission was coupled into a Princeton Instruments SP-2300i spectrometer, equipped with a Thorlabs LC100/M CCD detector array (0.14 nm resolution). Fast Fourier Transform (FFT) analysis of random lasing mode patterns for large arrays of pump laser shots was performed using the Gwyddion software package. The laser beam intensity profiles were analysed by a LabMax-TOP camera from Coherent Inc.

References

1. Gratzel, M. The light and shade of perovskite solar cells. *Nat. Mater.* **13,** 838–842 (2014).
2. Green, M. A., Ho-Baillie, A. & Snaith, H. J. The emergence of perovskite solar cells. *Nat. Photon.* **8,** 506–514 (2014).
3. Park, N. G. Organometal perovskite light absorbers toward a 20% efficiency low-cost solid-state mesoscopic solar cell. *J. Phys. Chem. Lett.* **4,** 2423–2429 (2013).
4. Zhou, H. *et al.* Interface engineering of highly efficient perovskite solar cells. *Science* **345,** 542–546 (2014).
5. Chung, I., Lee, B., He, J., Chang, R. P. & Kanatzidis, M. G. All-solid-state dye-sensitized solar cells with high efficiency. *Nature* **485,** 486–489 (2012).
6. Stranks, S. D. *et al.* Electron-hole diffusion lengths exceeding 1 micrometer in an organometal trihalide perovskite absorber. *Science* **342,** 341–344 (2013).
7. Xing, G. *et al.* Long-range balanced electron- and hole-transport lengths in organic-inorganic $CH_3NH_3PbI_3$. *Science* **342,** 344–347 (2013).
8. Nie, W. *et al.* High-efficiency solution-processed perovskite solar cells with millimeter-scale grains. *Science* **347,** 522–525 (2015).
9. Dong, Q. *et al.* Electron-hole diffusion lengths $>$ 175 um in solution-grown $CH_3NH_3PbI_3$ single crystals. *Science* **347,** 967–970 (2015).
10. Shi, D. *et al.* Low trap-state density and long carrier diffusion in organolead trihalide perovskite single crystals. *Science* **347,** 519–522 (2015).
11. Zhang, F. *et al.* Brightly luminescent and color-tunable colloidal CH3NH3PbX3 (X = Br, I, Cl) quantum dots: potential alternatives for display technology. *ACS Nano* **9,** 4533–4542 (2015).
12. Jeon, N. J. *et al.* Compositional engineering of perovskite materials for high-performance solar cells. *Nature* **517,** 476–480 (2015).
13. Dou, L. *et al.* Solution-processed hybrid perovskite photodetectors with high detectivity. *Nat. Commun.* **5,** 5404 (2014).
14. Guo, Y. L., Liu, C., Tanaka, H. & Nakamura, E. Air-stable and solution-processable perovskite photodetectors for solar-blind UV and visible light. *J. Phys. Chem. Lett.* **6,** 535–539 (2015).
15. Yakunin, S. *et al.* Detection of X-ray photons by solution-processed lead halide perovskites. *Nat. Photon.* **9,** 444–449 (2015).
16. Tan, Z. K. *et al.* Bright light-emitting diodes based on organometal halide perovskite. *Nat. Nanotechnol.* **9,** 687–692 (2014).
17. Sutherland, B. R., Hoogland, S., Adachi, M. M., Wong, C. T. & Sargent, E. H. Conformal organohalide perovskites enable lasing on spherical resonators. *ACS Nano* **8,** 10947–10952 (2014).
18. Xing, G. *et al.* Low-temperature solution-processed wavelength-tunable perovskites for lasing. *Nat. Mater.* **13,** 476–480 (2014).
19. Zhang, Q., Ha, S. T., Liu, X., Sum, T. C. & Xiong, Q. Room-temperature near-infrared high-Q perovskite whispering-gallery planar nanolasers. *Nano Lett.* **14,** 5995–6001 (2014).
20. Deschler, F. *et al.* High photoluminescence efficiency and optically pumped lasing in solution-processed mixed halide perovskite semiconductors. *J. Phys. Chem. Lett.* **5,** 1421–1426 (2014).
21. Zhu, H. *et al.* Lead halide perovskite nanowire lasers with low lasing thresholds and high quality factors. *Nat. Mater.* **14,** 636–642 (2015).
22. Protesescu, L. *et al.* Nanocrystals of cesium lead halide perovskites (CsPbX, X = Cl, Br, and I): novel optoelectronic materials showing bright emission with wide color gamut. *Nano Lett.* **15,** 3692–3696 (2015).
23. Oga, H., Saeki, A., Ogomi, Y., Hayase, S. & Seki, S. Improved understanding of the electronic and energetic landscapes of perovskite solar cells: high local charge carrier mobility, reduced recombination, and extremely shallow traps. *J. Am. Chem. Soc.* **136,** 13818–13825 (2014).
24. Sharma, S., Weiden, N. & Weiss, A. Phase diagrams of quasibinary systems of the type: ABX_3-$A'BX_3$; ABX_3 - $AB'X_3$ and ABX_3 - ABX'_3; X = halogen. *Z. Phys. Chem.* **175,** 63–80 (1992).
25. Trots, D. M. & Myagkota, S. V. High-temperature structural evolution of caesium and rubidium triiodoplumbates. *J. Phys. Chem. Solids* **69,** 2520–2526 (2008).
26. Stoumpos, C. C., Malliakas, C. D. & Kanatzidis, M. G. Semiconducting tin and lead iodide perovskites with organic cations: phase transitions, high mobilities, and near-infrared photoluminescent properties. *Inorg. Chem.* **52,** 9019–9038 (2013).
27. Wang, Y. *et al.* Blue liquid lasers from solution of CdZnS/ZnS ternary alloy quantum dots with quasi-continuous pumping. *Adv. Mater.* **27,** 169–175 (2015).
28. Dang, C. *et al.* Red, green and blue lasing enabled by single-exciton gain in colloidal quantum dot films. *Nat. Nanotechnol.* **7,** 335–339 (2012).
29. Dang, C. & Nurmikko, A. Beyond quantum dot LEDs: optical gain and laser action in red, green, and blue colors. *MRS Bull.* **38,** 737–742 (2013).
30. Chen, O. *et al.* Compact high-quality CdSe–CdS core–shell nanocrystals with narrow emission linewidths and suppressed blinking. *Nat. Mater.* **12,** 445–451 (2013).
31. Carbone, L. *et al.* Synthesis and micrometer-scale assembly of colloidal CdSe/CdS nanorods prepared by a seeded growth approach. *Nano Lett.* **7,** 2942–2950 (2007).
32. Mahler, B., Nadal, B., Bouet, C., Patriarche, G. & Dubertret, B. Core/shell colloidal semiconductor nanoplatelets. *J. Am. Chem. Soc.* **134,** 18591–18598 (2012).
33. Lhuillier, E. *et al.* Two-dimensional colloidal metal chalcogenides semiconductors: synthesis, spectroscopy, and applications. *Acc. Chem. Res.* **48,** 22–30 (2015).
34. Grim, J. Q. *et al.* Continuous-wave biexciton lasing at room temperature using solution-processed quantum wells. *Nat. Nanotechnol.* **9,** 891–895 (2014).
35. She, C. *et al.* Low-threshold stimulated emission using colloidal quantum wells. *Nano Lett.* **14,** 2772–2777 (2014).
36. Robel, I., Gresback, R., Kortshagen, U., Schaller, R. D. & Klimov, V. I. Universal size-dependent trend in auger recombination in direct-gap and indirect-gap semiconductor nanocrystals. *Phys. Rev. Lett.* **102,** 177404 (2009).
37. Klimov, V. I. *et al.* Optical gain and stimulated emission in nanocrystal quantum dots. *Science* **290,** 314–317 (2000).
38. Coldren, L. A., Corzine, S. W. & Mašanović, M. L. in *Diode Lasers and Photonic Integrated Circuits* 247–333 (John Wiley & Sons, Inc., 2012).
39. Shaklee, K. L. & Leheny, R. F. Direct determination of optical gain in semiconductor crystals. *Appl. Phys. Lett.* **18,** 475–477 (1971).
40. Grivas, C. *et al.* Single-mode tunable laser emission in the single-exciton regime from colloidal nanocrystals. *Nat. Commun.* **4,** 2376 (2013).
41. Xing, G. *et al.* Ultralow-threshold two-photon pumped amplified spontaneous emission and lasing from seeded CdSe/CdS nanorod heterostructures. *ACS Nano* **6,** 10835–10844 (2012).
42. Wiersma, D. S. The physics and applications of random lasers. *Nat. Phys.* **4,** 359–367 (2008).
43. Laubsch, A., Sabathil, M., Baur, J., Peter, M. & Hahn, B. High-power and high-efficiency InGaN-based light emitters. *IEEE Trans. Electron Devices* **57,** 79–87 (2010).
44. Ithurria, S. *et al.* Colloidal nanoplatelets with two-dimensional electronic structure. *Nat. Mater.* **10,** 936–941 (2011).
45. Tessier, M. D. *et al.* Efficient exciton concentrators built from colloidal core/crown CdSe/CdS semiconductor nanoplatelets. *Nano Lett.* **14,** 207–213 (2014).
46. Leatherdale, C. A., Woo, W. K., Mikulec, F. V. & Bawendi, M. G. On the absorption cross section of CdSe nanocrystal quantum dots. *J. Phys. Chem. B* **106,** 7619–7622 (2002).
47. Kunneman, L. T. *et al.* Nature and decay pathways of photoexcited states in CdSe and CdSe/CdS nanoplatelets. *Nano Lett.* **14,** 7039–7045 (2014).
48. Dhanker, R. *et al.* Random lasing in organo-lead halide perovskite microcrystal networks. *Appl. Phys. Lett.* **105,** 151112 (2014).
49. Namdas, E. B. *et al.* Low thresholds in polymer lasers on conductive substrates by distributed feedback nanoimprinting: progress toward electrically pumped plastic lasers. *Adv. Mater.* **21,** 799–802 (2009).

50. Kozlov, V. G., Bulovic, V., Burrows, P. E. & Forrest, S. R. Laser action in organic semiconductor waveguide and double-heterostructure devices. *Nature* **389,** 362–364 (1997).
51. Thijs, P. J. A., Tiemeijer, L. F., Kuindersma, P. I., Binsma, J. J. M. & Van Dongen, T. High-performance 1.5 mu m wavelength InGaAs-InGaAsP strained quantum well lasers and amplifiers. *IEEE J. Sel. Top. Quantum Electron.* **27,** 1426–1439 (1991).
52. Klimov, V. I. *et al.* Single-exciton optical gain in semiconductor nanocrystals. *Nature* **447,** 441–446 (2007).
53. Cao, H. Lasing in random media. *Waves Random Media* **13,** R1–R39 (2003).
54. Redding, B., Choma, M. A. & Cao, H. Speckle-free laser imaging using random laser illumination. *Nat. Photon.* **6,** 355–359 (2012).
55. Redding, B. *et al.* Low spatial coherence electrically pumped semiconductor laser for speckle-free full-field imaging. *Proc. Natl Acad. Sci. USA* **112,** 1304–1309 (2015).
56. Reidler, I., Aviad, Y., Rosenbluh, M. & Kanter, I. Ultrahigh-speed random number generation based on a chaotic semiconductor laser. *Phys. Rev. Lett.* **103,** 024102 (2009).

Acknowledgements

M.V.K. acknowledges financial support from the European Union through the FP7 (ERC Starting Grant NANOSOLID, GA No. 306733). W.H. is grateful to the Austrian Science Foundation (FWF) for financial support via the SFB project IR_ON. Ehsan Hassanpour Yesaghi and Sebastian Manz are acknowledged for technical assistance in the laser lab. We thank Nadia Schwitz for help with photography of the emission from CsPbX3 solutions, Dr. Dmitry Dirin for syntesis of CdSe and CdSe/CdS nanoplatelets and Dr. Nicholas Stadie for reading the manuscript.

Author contributions

M.V.K. conceived and initiated the work. S.Y., M.H. and W.H. performed the ASE and lasing measurements; S.Y. analysed the ASE/lasing results; L.P. and F.K. synthesized the $CsPbX_3$ NCs; M.I.B. collected the transmission electron microscopy images; G.D.L. and M.F. provided fs and ns laser setups and technical advice; M.V.K., W.H. and M.F. supervised the work. S.Y. and M.K. wrote the manuscript. All authors discussed the results and commented on the manuscript.

Additional information

Supplementary Information accompanies this paper at http://www.nature.com/naturecommunications

Competing financial interests: The authors declare no competing financial interests.

Reprints and permission information is available online at http://npg.nature.com/reprintsandpermissions/

How to cite this article: Yakunin, S. *et al.* Low-threshold amplified spontaneous emission and lasing from colloidal nanocrystals of caesium lead halide perovskites. *Nat. Commun.* 6:8056 doi: 10.1038/ncomms9056 (2015).